IOP Publishing Classical and Quantum Gravity
Class. Quantum Grav. **39** (2022) 025009 (31pp) https://doi.org/10.1088/1361-6382/ac1be4

Newtonian-noise characterization at Terziet in Limburg—the Euregio Meuse–Rhine candidate site for Einstein Telescope

Maria Bader[1,5], Soumen Koley[1,2,*], Jo van den Brand[1,3,5], Xander Campman[4], Henk Jan Bulten[1,5], Frank Linde[1,6] and Bjorn Vink[7]

[1] Nikhef, Science Park, 1098 XG Amsterdam, The Netherlands
[2] Gran Sasso Science Institute (GSSI), I-67100 L'Aquila, Italy
[3] Maastricht University, 6211 LK Maastricht, The Netherlands
[4] Shell Global Solutions International B.V., The Netherlands
[5] Vrije Universiteit Amsterdam, 1081 HV Amsterdam, The Netherlands
[6] University of Amsterdam, 1012 WX Amsterdam, The Netherlands
[7] Antea Group B.V., The Netherlands

E-mail: skoley@nikhef.nl

Received 1 June 2021, revised 20 July 2021
Accepted for publication 9 August 2021
Published 11 January 2022

Abstract

Limburg, in the border region between Belgium, Germany and the Netherlands, has been identified as the Euregio Meuse–Rhine candidate site for Einstein Telescope. The site hosting this gravitational-wave observatory must minimize the Newtonian coupling of ground vibrations to the core optics of the low-frequency detectors. Newtonian noise depends on the ambient seismic field which is in turn dependent on the site's geology and the distribution of surface and underground seismic-noise sources. We have characterized the site near Terziet in Limburg in terms of propagation modes, dispersion and angular distribution of seismic noise by employing sensor arrays on the surface. Attenuation of seismic noise with depth was studied with a borehole sensor. Based on the results of these measurements, a realistic seismic-field model has been derived that represents a complete solution of the elastodynamic wave equations for a horizontally-layered soil structure. This seismic-field model allows to estimate the Newtonian-noise contribution to the sensitivity of Einstein Telescope for the characteristic geology and ambient noise conditions in South Limburg. The site's geology features soft-soil layers on hard-rock and is effective in attenuating Newtonian noise from surface waves below the required sensitivity.

*Author to whom any correspondence should be addressed.

A random background of body waves with all possible angles of incidence is expected to constitute the dominant source of Newtonian noise.

Keywords: Newtonian-noise, Einstein Telescope, surface waves, background body-wavesseismic noise

(Some figures may appear in colour only in the online journal)

1. Introduction

The era of gravitational-wave science was firmly established with the detection of several signals from coalescing binary black holes [1–7] and neutron star binaries [6–8]. The currently operating gravitational-wave detectors include Advanced LIGO [9], Advanced Virgo [10], and KAGRA [11], and these ground-based laser interferometers are sensitive in the frequency band from about 10 Hz to 10 kHz.

Einstein Telescope [12] is an advanced gravitational-wave observatory, in the planning stage, that aims to improve the strain sensitivity by one order of magnitude compared to the present performance of the LIGO and Virgo detectors [7]. This will allow detection of hundreds of gravitational-wave events per day with events originating from times as early as the cosmic dark ages of the Universe. Einstein Telescope at its design sensitivity will allow measuring the mergers of binary neutron stars at redshifts higher than 10 and mergers of binary black holes to a redshift of up to 100 [13]. As the signals of these distant events will be strongly redshifted, Einstein Telescope aims at extending the low-frequency limit of gravitational-wave detection to as low as 2 Hz.

A possible location to host Einstein Telescope is the Euregio Meuse–Rhine (EMR) which comprises the cities of Aachen in Germany, Liège in Belgium, and Maastricht in the Netherlands. The potential site will be located near the village Terziet in Limburg, the southernmost province of the Netherlands (see figure 1). It is a rural area with a population density of about 40 persons per square kilometer [14], and is designated as a ‘quiet zone’. The area is known for its tranquillity, agricultural activity and tourism. The EMR-site is in the heart of the Leuven–Aachen–Eindhoven triangle, a European top technology area with numerous universities, established high-tech companies, while all necessary infrastructure is easily available.

The local geology and the environmental conditions of the site are important, as the performance of terrestrial interferometric gravitational-wave detectors at frequencies below about 20 Hz is limited by seismic noise [15]. It couples to the test masses (i.e. the main mirrors of the interferometers) in two ways, mechanically by moving the mirror suspensions and directly by gravitational attraction. Experience at Virgo has shown that the mechanical coupling of the ground motion can be suppressed efficiently by several orders of magnitude through advanced vibration–isolation systems [16]. However, the Newtonian force on the test masses, created by seismically-induced mass–density fluctuations, cannot be shielded or easily suppressed. This effect on the detector sensitivity was first identified by Rainer Weiss in 1972 [17] and is referred to as Newtonian noise [15] (it is also known as gravity-gradient noise).

To minimize seismic and Newtonian noise, the EMR-site, if chosen, will host Einstein Telescope a few hundred meters underground. The observatory will then be constructed in hard-rock as this offers many advantages for the realization of tunnels and caverns. The geology characteristic for Limburg features soft-soil layers covering the hard-rock, and we will show that this layered geology is effective in suppressing Newtonian noise generated at the surface. Firstly, the impedance differences of the various layers lead to reflections at the layer-interfaces of the seismic energy that is generated at the surface (e.g. due to human activity

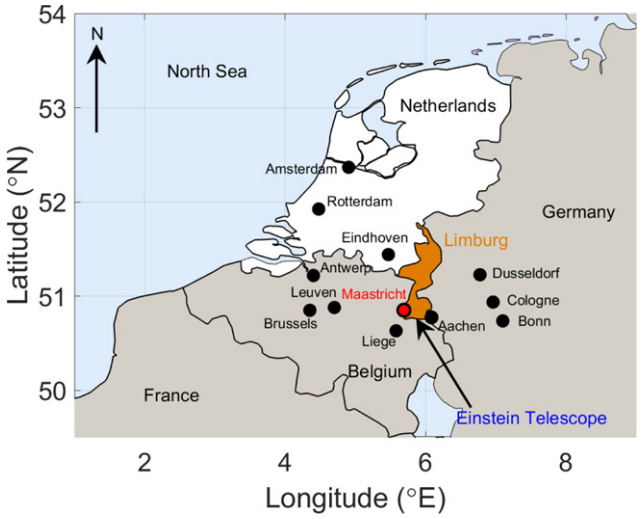

Figure 1. The EMR candidate site for Einstein Telescope is located in Limburg, in the south of the Netherlands near the border with Belgium and Germany.

in nearby villages, on roads, and due to farming). This rock stratification causes the seismic-noise power to be constrained to the near-surface soil layers, with only a small fraction of noise power reaching locations near the sensitive test masses. Secondly, the seismic waves near the surface are highly dispersive and have short wavelengths in the soft-soil layers. These Rayleigh and Love waves attenuate strongly with depth, and at high frequency, these horizontally traveling waves attenuate even more strongly due to inelastic effects. In addition, these surface waves have relatively short wavelength and this leads to cancellation effects when summing the Newtonian noise on a test mass over kilometer-scale integration bounds. Thirdly, the seismic waves will have high velocity in the deep hard-rock layers and will consequently have lower amplitudes. This causes underground tunnel and cavern walls to experience only small displacements, leading to relatively low Newtonian-noise contributions from nearby structures.

The first quantitative analysis was carried out by Peter Saulson in 1984 [18] who considered terrestrial gravitational noise due to displacements from seismic waves and due to air-pressure fluctuations. We neglect the latter as Newtonian noise from atmospheric pressure variations has been treated e.g. in [19]. We also do not consider Newtonian-noise suppression based on shaping of the local topography near gravitational-wave observatories [20]. Estimates of the seismic Newtonian noise for a given detector rely on a model of the geology and on the seismic field near the test masses. As seismic noise for frequencies from about 1 to 20 Hz is dominated by anthropogenic noise, several authors assume only surface-wave contributions in their wave-field models. In these analytic models the main surface contributions are considered to be either Rayleigh waves [21, 22] or a combination of Rayleigh and Love waves [23]. The restriction to surface waves was employed, since neither a detailed geological model of the subsurface at the detector site nor the realistic distribution of noise sources and their spectral content was available. Together with finite-element models of underground seismic fields in homogeneous media [22, 24–27], these early studies stress the necessity of a detailed seismic model.

In order to establish the quality of the EMR-site, we have characterized the local geology [26, 28–32]. Section 2 discusses borehole logging that provided a lithographic interpretation of the subsurface. Passive seismic sensor-array studies provide Rayleigh-wave dispersion

curves for both fundamental and higher-order modes. These data, together with the lithographic information, are used in an inversion to obtain a five-layer subsurface model providing layer thickness, density, and P- and S-wave speeds. Active seismic sensor-array studies were carried out and allowed a refraction analysis to obtain a P-wave model. A tri-axial surface sensor was used to determine the ratio of horizontal to vertical seismic-noise amplitude. A second tri-axial sensor measured seismic noise at 250 m depth in a borehole. Besides geology, the spatio-spectral properties of seismic noise must be known to solve the wave equation for a realistic multi-layered, seismically excited medium. To this end we performed a beamforming analysis of passive sensor-array data. Section 3 discusses how the above information yields a displacement field that represents the full solution to the elastodynamic wave equations for the EMR-site. This solution includes all wave types (surface Rayleigh and Love waves, and body P- and S-waves) and accounts for attenuation and reflection, refraction, and mode-conversion at layer boundaries. The calculation of Newtonian noise is presented in Section 4. The displacement field is integrated over the various layers and takes boundaries and spherical caverns into account. Contributions from both ambient surface and a random body-wave background are accounted for. The consequences for the sensitivity of Einstein Telescope at the EMR-site are discussed. The main conclusions are summarized in Section 5.

2. Site characterization studies

The EMR-site has been characterized between 2017 and 2020 by means of several passive and active seismic-array studies and two borehole campaigns. Rock samples were collected to a depth of 140 m and resulted in a lithology model. Passive studies employed seismic sensors to monitor the ambient noise, whereas in active studies the surface was excited with a seismic source and the response to this excitation was recorded by an array of receivers. These studies allowed to obtain a detailed understanding of the local noise source distribution. Moreover, they allowed to characterize the subsurface geology. Coincident power spectral density (PSD) measurements were carried out on the surface and at 250 m depth, and provided information on attenuation and horizontal to vertical spectral-amplitude ratios. In the following sections we will list the most relevant outcome of these studies. For a complete list of all seismic studies and their results the reader is referred to [25, 26, 28–32].

2.1. Lithology model from borehole logging

In March 2017 a borehole with a diameter of 270 mm and a depth of 140 m was drilled near the village Terziet in South Limburg, the Netherlands at 50°45′22.6″ latitude and 5°54′24.2″ longitude. To plan and execute this project we collaborated with industrial partners such as Innoseis [33], Deltares [34], Toegepast Natuurwetenschappelijk Onderzoek [35], and Energie Beheer Nederland [36]. During the drilling process rock samples were collected and stored every 5 m. Moreover, standard borehole logging techniques of exploration geophysics [37] have been applied to gain information about the subsurface geology and lithology [39, 40]. These include the following geophysical techniques:

Resistivity logging: We measured the single point resistivity (SPR) by determining the electrical resistance from points within the borehole to an electrical ground on the surface. Moreover, we measured the resistivity along the borehole by determining the potential with an electrode at a fixed position (SHNO[8]) while a second electrode (LONO[9]) was moved upwards

[8] Short normal resistivity log.

[9] Long normal resistivity log, http://wellog.com/webinar/interp_gp1_gp6.htm.

in the borehole. The SHNO measurement allowed a maximum distance of 0.5 m between the electrodes, whereas the LONO measurement allowed a spacing of 0.8 to 1.6 m. The resistivity gives information about the porosity of the rock formation along the borehole, as saline water leaks from pores in the rock into the borehole water. The higher the porosity of the material, the higher the conductivity of the water in the borehole between the electrodes and the lower the resistivity [41].

Gamma-ray (GR) logging: With GR logging [37] the natural gamma radiation emitted by the subsurface rock along the borehole is measured. Values from about 75 to 200 gAPI (gamma ray API unit) [38] indicate the presence of clay-rich rock formations such as shale, claystone or mudstone, whereas values around 20 gAPI are an indicator for clean or coarse-grained sandstone and carbonate rock, such as dolomite and limestone. The GR spectrum can only serve as an indicator for the clay content of the rock formation and has to be combined with other data to make more precise statements about the subsurface lithology. Distinguishing the contribution of potassium (K), uranium (U) and thorium (Th) to the GR spectrum is a powerful tool. Thorium is typically associated with shales and heavy minerals containing zinc and lead, while potassium is present mainly in shale rock and stabilizes clay minerals. Uranium can be linked to organic matter content in the rock [42].

Sonic logging: The sonic logging tool had a length of 3.5 m and consisted of a sonic pulse emitter at the top, one receiver nearby the emitter and one receiver at the bottom of the tool. When a short-period high-amplitude sonic pulse is emitted (we employed a 10 kHz signal), it excites seismic waves in the surrounding rock structure which are measured by the receivers. In this manner the P-wave velocity of the subsurface can be derived. Velocities smaller than 2.0 km s^{-1} indicate non-saturated soft materials while velocities higher than 2.5 km s^{-1} indicate hard-rock material.

Results from borehole logging [40] are shown in figure 2. The GR measurements were carried out with different tools and show consistent results. The increase in GR level after 10 m and the decrease after 35 m, as well as the change in resistivity at 90 m indicate the start of new soil layers. The sonic log shows the P-wave speed measured by using the borehole compensated travel-time that is measured by using the difference in travel-time of the emitted pulse at a nearby and a far-away receiver located at different subsurface depths.

The results from borehole logging and the analysis of soil samples allow the following lithographic interpretation:

0–5 m: Surface rock samples collected during the preparation of the borehole site revealed a thin surface layer of pure clay material to a depth of about 5 m. Slight variations in the GR spectra and in the velocity spectra after 5 m indicate the presence of a new material layer.

5–10 m: Changes in Th and U GR levels indicate a new material layer, and the lower GR levels show that the clay content in this layer is reduced. The low resistivity indicates a highly porous, soft-rock material. However, high-velocity spikes in the P-wave speed hints to hard-rock gravel material. Soft material at these shallow depths typically originate from the Cretaceous, a geological period that lasted from 145 to 66 million years ago. The main material of this layer consists of lightweight sandstone and is part of the Beusdael member of the Vaals formation.

10–15 m: The wave speed and resistivity in this layer are still low, which indicates a soft material. At about 12 m the GR level and K and Th contributions drastically increase, signaling a change of material. In this layer the transition from soft-soil to hard-rock manifests itself as a fine, grainy mix of silt-stones. While the GR properties change at 12 m due to the presence of soft weathered carboniferous rock, seismic wave propagation is governed by the

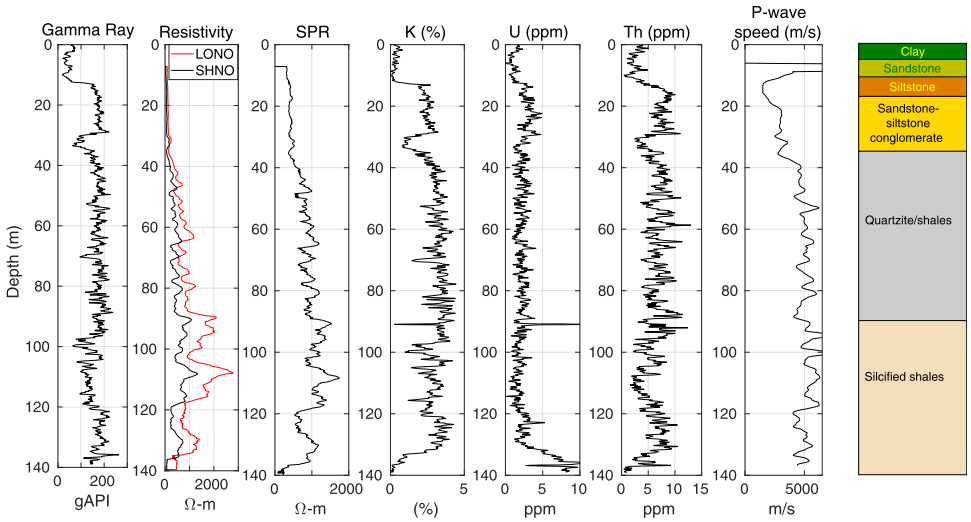

Figure 2. Borehole logging to a depth of 140 m showing the GR level, resistivity from short (SHNO) and long normal (LONO) measurements, and SPR. Also shown are the GR spectrum decomposed into contributions from the elements K, U and Th. Sonic logging was used to obtain the P-wave speed. The right column shows the lithographic interpretation of the subsurface based on these data.

mechanical properties of the medium which do not significantly change. Since the latter are important for the inversion, we treat 10 to 15 m as a single layer.

15–35 m: The overall increasing, but yet fluctuating wave speed of this layer indicates a large amount of gravel and hard-rock material. Nevertheless, the material shows low resistivity, indicating the presence of soft material and rough gravel. The high GR-level indicates that the soft material in this layer is clay whereas the Th and K contents are typical for sandstone. This layer is a coarse-grained rock conglomerate with fine white pebbles, consisting of various sandstone and clay materials. These formations look similar to the Burgholz conglomerates of the lower Namurian found south of Aachen.

35–90 m: This layer is characterized by a clear change in GR level at 35 m, the increase in resistivity, meaning a decrease of rock porosity and an increase in wave speed to velocities above 4 km/s; all indicating a hard-rock material. This section belongs to the Evieux-formation originating from the upper-Famennian and breaks through the surface near Val Dieu, 8 km west–south–west of Terziet. It consists of many 0.1 m–0.5 m thin, strongly folded and faulted layers. The fault structure is also seen in the fluctuating Th spectrum. Thorium is often combined with heavy minerals such as lead and zinc, which are components of the formations present in this area. Each thin layer consists of different amounts of minerals, leading to a fluctuation in the Th spectrum. At a depth of 92 m a strong peak in the U and K levels indicates the folding of a layer with shale content, originating from greater depths.

90–140 m: At a depth of 90 m the resistivity drastically increases, which indicates the presence of a hard-rock formation. The reduction of the GR-level indicates the presence of shale. This section belongs probably to the Monfort-formation. Since it is difficult to separate this layer from the upper-lying Evieux-formation, these formations are normally combined as ‘Monfort–Evieux’ on the official Belgium geological maps. The separation between those

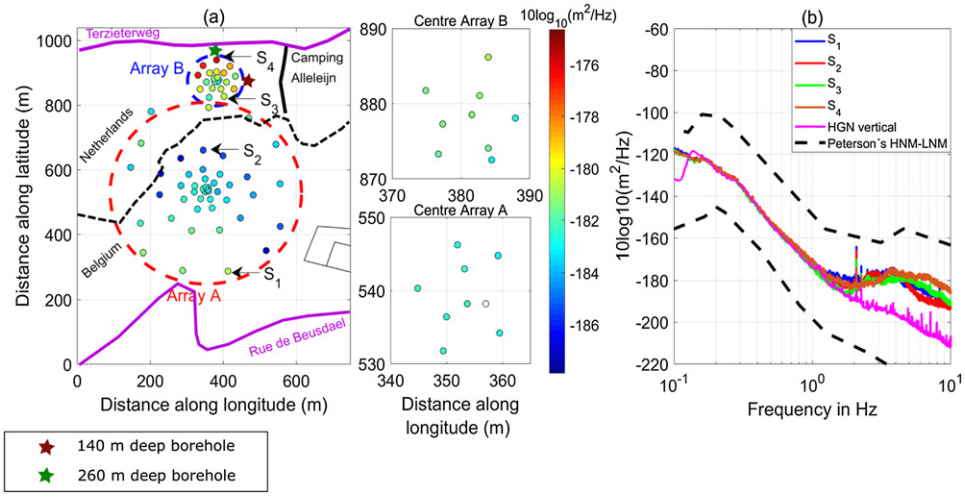

Figure 3. Left: layout of the passive sensor array. Each circular marker indicates the location of a seismometer, its color shows the PSD averaged from 1 to 10 Hz over the period November 4 to 28, 2017. For clarity, the closely spaced seismometers located in the inner two rings of each of the arrays are also shown. The red and the green stars point to the location of the two boreholes drilled at the site. The PSD of sensors S1 to S4 are displayed in the right panel. Right: sensors S1 and S2 in Array A exhibit a higher noise level (PSD mode) between 1 Hz and 3 Hz than sensors S3 and S4 in Array B. For comparison, the PSD at the nearby KNMI Heimansgroeve observatory (HGN) constructed on an outcrop is shown in magenta. Above about 3 Hz the HGN PSD spectrum is up to two orders of magnitude lower with respect to the surface-array data. The black-dashed curves represent Peterson's new low- and high-noise models.

layers might be related to an event horizon that might be marked by the U-spike at 92 m depth. Monfort contains less radioactive layers with coaled plant fossils than Evieux.

The lithology interpretation is not trivial and we have collaborated with experts of the local geology to obtain an overall understanding of the subsurface composition. The lithology allows to group the subsurface stratification into three main zones: a soft material layer on the surface (0 m–15 m), laying on a hard-rock bedrock (35 m to at least 140 m) with a mostly soft, thin transition zone in between (15 m–35 m).

2.2. Geology model and surface seismic noise from sensor-array studies

From November 4 to 28, 2017 a network of 74 seismic sensors was deployed in two arrays (see figure 3, left panel) near the village of Terziet in Limburg, the Netherlands [28].

PSD values averaged over all days of measurement between November 4 to 28, 2017 and averaged in the frequency band between 1 and 10 Hz are computed and are shown as a function of the seismometer locations in figure 3, left panel. Four representative PSDs averaged over a day of measurement (November 11, 2017) from individual sensors are shown in figure 3, right panel. Due to the remote location, the surface-array spectra are relatively quiet. For reference the black-dashed curves represent Peterson's new low- and high-noise models [43]. For the same period, data were recorded with an STS1 seismometer [44] at the HGN seismic station located on an outcrop where the hard-rock layer is exposed on the surface. The HGN station is about 1 km to the north–east of the sensor array. Below 1 Hz, where microseismic activity is

dominant, the vertical spectra from the array and the STS-1 are in excellent agreement. Above 1 Hz, where noise is created by anthropogenic activity, the PSD at HGN is already suppressed by up to two orders of magnitude with respect to surface data. This is because the surface array is placed on the soft-soil layer, while the STS-1 is installed on the hard-rock layer.

We employed beamforming which is a passive seismic data analysis method for estimating the surface wave propagation attributes. The beampower $B(f)$ at a frequency of interest f is estimated for different values of slowness (p_k) and azimuth (θ_k), and can be expressed as

$$B(p_k, \theta_k, f) = \frac{1}{N} w_k R_{xx}(f) w_k^*, \tag{2.1}$$

where N represent the number of time windows of the data which is used for computing the frequency domain data covariance matrix $R_{xx}(f)$ and '*' represents the complex conjugate operator. The steering vector $w_k(f)$ is expressed as $w_k(f) = [\mathrm{e}^{-\mathbf{i}2\pi f\tau_0}, \mathrm{e}^{-\mathbf{i}2\pi f\tau_1}, \ldots, \mathrm{e}^{-\mathbf{i}2\pi f\tau_{M-1}}]$ where $\mathbf{i} = \sqrt{-1}$ and $\tau_m = x_m p_k \cos\theta_k + y_m p_k \sin\theta_k$ is the time delay for a plane wave propagating with slowness p_k and along an azimuth θ_k to reach the seismometer located at coordinates (x_m, y_m) [45]. The circular design of the arrays allows to resolve seismic waves arriving from all directions. With beamforming [28, 45] the direction of incidence θ of the surface waves and their slowness p (i.e. the inverse of the velocity) has been determined. The frequency resolution of each array is determined by the number of rings and their radius. It can be shown that for simple and regular array geometries the resolving power is related to the minimum and maximum inter-sensor spacing [46]. Array A had a maximum aperture of 512 m and consisted of seven rings with 49 sensors in total. Its sensitive frequency range for beamforming was from 2.4 to 14.0 Hz. Array B was smaller with a maximum aperture of 112 m and was comprised of five rings with 25 sensors. Due to its smaller diameter, Array B was sensitive for beamforming in the frequency range of 3.0–14.0 Hz.

Beamforming shows that the main seismic-noise sources for both arrays are local and in close vicinity of the sensor array (figure 4). If the sources would be far away, then the beampower distribution derived for Array A and B would be similar. However, this is not observed in the data. Figure 4 shows that the distributions differ for Array A and B (for example at frequencies 4.2, 5.8, and 7.0 Hz) indicating the presence of sources in the vicinity of the arrays. For Array A, the main noise in the whole frequency band originates from the south–western direction, most likely from traffic on the Rue de Beusdael (see figure 3, left panel). For increasing frequency the incoming noise is not as localized and spreads over a large angle anticlockwise from the western to the eastern direction, where a farm is located about 200 m from the center of the array. At low frequencies, Array B picks up noise from Rue de Beusdael as well, but the signal is dominated by ambient noise from the northern direction. As the frequency increases, the noise originates from the northern direction and in addition starts to spread toward east. Possible noise sources are the Terzieterweg and the nearby camping ground (see figure 3, left panel).

The peak of the beampower distribution in the radial direction indicates for each frequency the surface-wave velocity. Array A resolves a larger frequency range, and was therefore used to determine the dispersion curve (figure 5, left panel). An additional advantage of the large aperture is that it allows to record not only the fundamental Rayleigh-wave mode, but also the first overtone above 5 Hz, visible as two slowness rings in the bottom plots of figure 4, left panel.

The presence of the first overtone can be understood by considering a medium with high, non-continuous velocity contrast in the subsurface composition, for example a thin, soft-soil layer on hard-rock as is the case in Limburg. The strength of overtones is determined by the excitation mechanism, e.g. the depth of the excitations. In principle overtones of surface waves

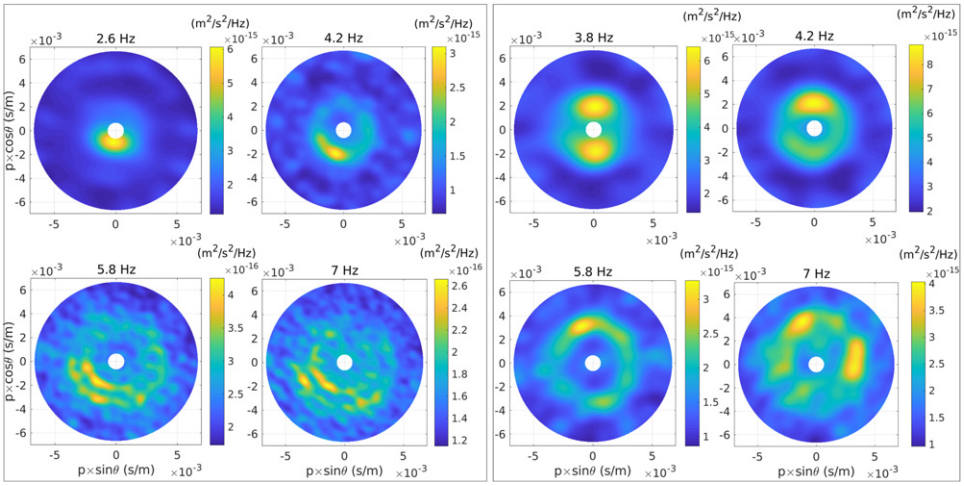

Figure 4. Selection of beamforming results for Array A (left panel) and Array B (right panel), analyzed during the same period. The radial axis displays the slowness p, and the azimuth angle θ is measured clockwise from the positive y-axis such that $x = p \cdot \sin\theta$ and $y = p \cdot \cos\theta$. The color scale indicates the normalized beampower. East is toward the positive x-axis, north toward the positive y-axis.

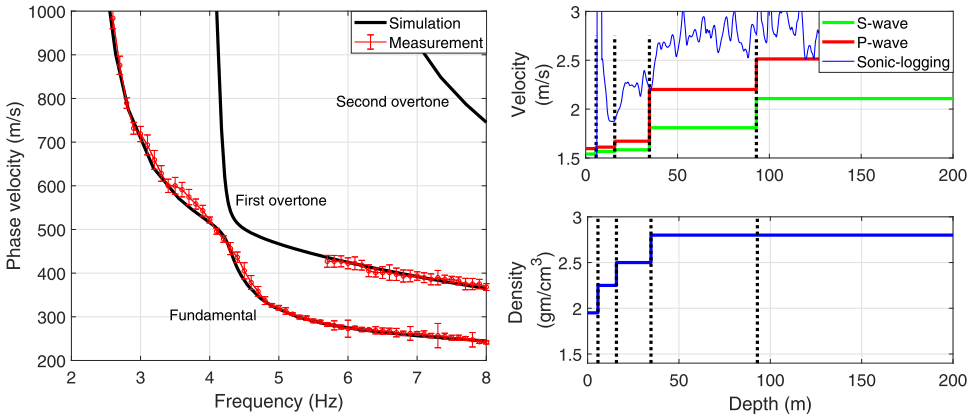

Figure 5. Left: dispersion curve of fundamental and first-overtone Rayleigh-wave propagation obtained from beamforming of Array A data compared to that of an inversion analysis. Both results are in excellent agreement. The error-bars in the measurement correspond to one standard deviation. Right: subsurface velocity and density model obtained from the inversion analysis. A steep velocity contrast at 35 m indicates the interface between soft-soil and hard-rock. Subsurface P-wave speeds obtained from sonic-logging are also shown for comparison. Note that sonic-logging at these shallow depths suffers from large uncertainties in P-wave velocity.

also exist in more homogeneous media [47]. However their amplitude is then very low, which makes it difficult to distinguish them from uncorrelated surface noise.

The fundamental and first-order Rayleigh-wave dispersion curves from Array A have been used in a parameter estimation for a non-linear forward problem to obtain a 1D-model of the

Table 1. Parameters for the five-layer subsurface model of the geology at the EMR-site derived from the inversion of the dispersion curve measured with Array A. The parameters are the layer thickness and density, and the P- and S-wave speeds.

Layer number	Thickness (m)	Density (10^3 kg m^{-3})	P-wave speed (km s^{-1})	S-wave speed (km s^{-1})
1	5.7	1.95	0.385	0.165
2	10.2	2.25	0.445	0.270
3	18.9	2.50	0.685	0.335
4	58.2	2.80	2.81	1.24
5	∞	2.80	4.05	2.43

subsurface lithology. This model is most representative at the center of Array A. The inversion has been carried out with a stochastic direct search method, where the parameter space contained the number of subsurface layers, as well as their thickness, density, and P- and S-wave speeds. With the subsurface information from the borehole study the inversion was based on six subsurface layers with the thickness and the densities from the lithology interpretation displayed in figure 2 as starting values [28]. The resulting model shows a steep velocity contrast at a depth of about 35 m, where the interface between soft-soil and hard-rock is located (figure 5, right panel). The parameters of the two layers from 5 to 10 m depth were found to be almost identical, making it more efficient to combine these layers.

The numerical values of the P- and S-wave speeds, and the density and thickness of each layer are summarized in table 1. The theoretical dispersion curve from these soil parameters is in good agreement with the measured dispersion curve (figure 5, left panel).

2.3. Seismic-noise attenuation and body-wave background

A second borehole was constructed at Terziet to a depth of 260 m and located at about 300 m toward the north–eastern direction from the center of Array A (figure 3). A tri-axial Trillium T240 seismometer measures ambient surface noise, and a tri-axial STS-5 broadband borehole seismometer is used to measure at a depth of 250 m. Long term measurements will provide information about annual variations of surface and underground seismic conditions.

The first set of simultaneous surface and underground data was taken from November 2019 to October 2020 (figure 6). At frequencies below 1 Hz noise mainly originates from microseismic activity. At these frequencies the wavelengths exceed 1 km, and for a depth of 250 m Rayleigh waves suffer little attenuation. Therefore, low-frequency surface and underground PSDs are about the same. As the frequency increases, horizontal and vertical displacements rapidly attenuate with depth. Rayleigh wavelengths above 4 Hz are shorter than 125 m at the EMR-site, and surface waves are attenuated strongly at the depth of the underground seismometer. Hence, the attenuation in power (ratio of PSDs) between surface and underground reaches a maximum of about four orders of magnitude above 4 Hz for horizontal and above 9 Hz for vertical PSDs (see figure 6, right panel). This difference in attenuation is explained by a dominant contribution from Rayleigh waves to the vertical component and from Love waves to the horizontal component.

The strong attenuation of seismic waves at the EMR-site is the result of the particular geology, where a layer of soft-soil is resting on hard-rock (see figure 2). Seismic waves above about 1 Hz are generated mostly by anthropogenic surface sources. As the waves travel through the subsurface, they are confined to the soft near-surface layers as they experience multiple reflections. Only a small fraction of the noise power generated at the surface, penetrates into the

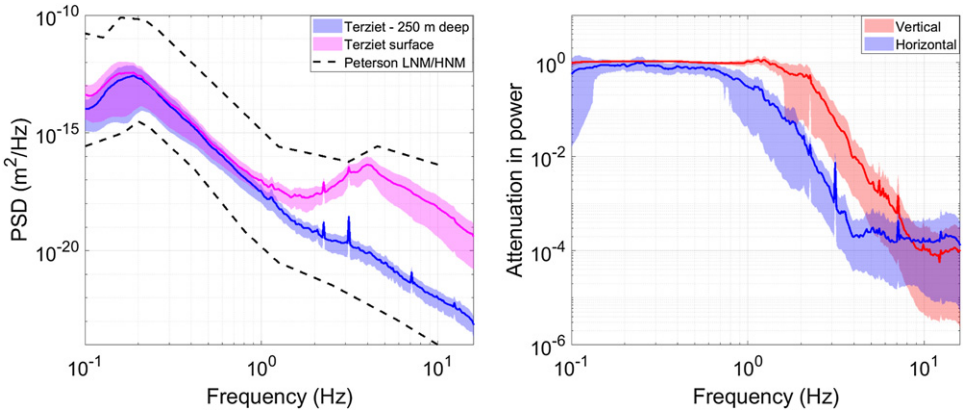

Figure 6. Left: horizontal displacement PSD measured from November 2019 to October 2020 in Terziet. The PSDs in north–south and east–west direction are the same. The solid curves show the mean of the PSD, while the shaded bands enclose the 10th and 90th percentiles. The PSD is shown together with Peterson's models for comparison. Right: attenuation of ambient seismic noise from surface to 250 m depth.

hard-rock layers. This means that at these frequencies, the vast majority of Rayleigh-wave power does not reach the borehole seismometer. This sensor then measures a combination of residual surface-wave noise and a random background of body-wave noise. The presence of this body-wave background, a superposition of body waves with all possible angles of incidence that arrive from unknown and relatively far-away surface and underground sources, has been quantified by investigating the temporal variation of surface and underground PSDs [30]. Seismic noise during the day is attenuated at a depth of 250 m by about a factor 10^4 in power. During the night-time the attenuation reduces to a factor of about 10^3 in power. This difference in attenuation between day- and night-time can be attributed to the presence of a continuous body-wave background. The contribution of the body-wave background at depth becomes significant during night-time due to the reduction of local sources of noise which generate mostly surface waves.

Figure 7 shows the estimated body-wave background for the horizontal and the vertical components of the ground motion. It has been shown that below 4 Hz, the body-wave background contributes about 25%–30% to the total underground noise and that above 4 Hz, the contribution of the body-wave background gradually increases to about 50% of the underground noise [30].

The tri-axial nature of the borehole seismometers allows to determine the ratio of horizontal (H) to vertical (V) noise amplitude spectral densities at the EMR-site (see figure 8). Note that the H-amplitude is given by the quadratic mean of the PSDs in the horizontal directions. The H–V spectral ratio is characteristic for a particular site as it depends on the local geology, and source depth and distance [48]. Moreover, it depends on the frequency, the specific wave type (in general a combination of P-, S-, Love, and Rayleigh waves), and the excitation mechanism of the source (e.g. horizontal versus vertical ground excitation).

Up to about 1 Hz the ratio at the borehole site is comparable for both sensors. Above 1 Hz anthropogenic activity, which is connected to surface excitations, is the dominant seismic noise source. Due to the high impedance contrast for soft-soil resting on hard-rock, the seismic amplitudes are confined to the surface layers and mode conversion is favored. As a result

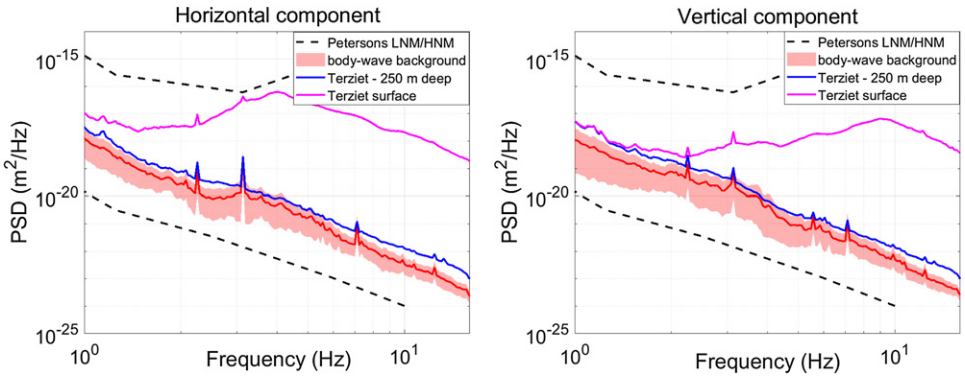

Figure 7. Left: PSD of the body-wave background corresponding to the horizontal component of seismic noise. The magenta and blue curves correspond to the seismic noise measured on the surface and underground, respectively. The red-shaded region shows the 10th and 90th percentiles over all analysis windows. Right: same as left but for the vertical component.

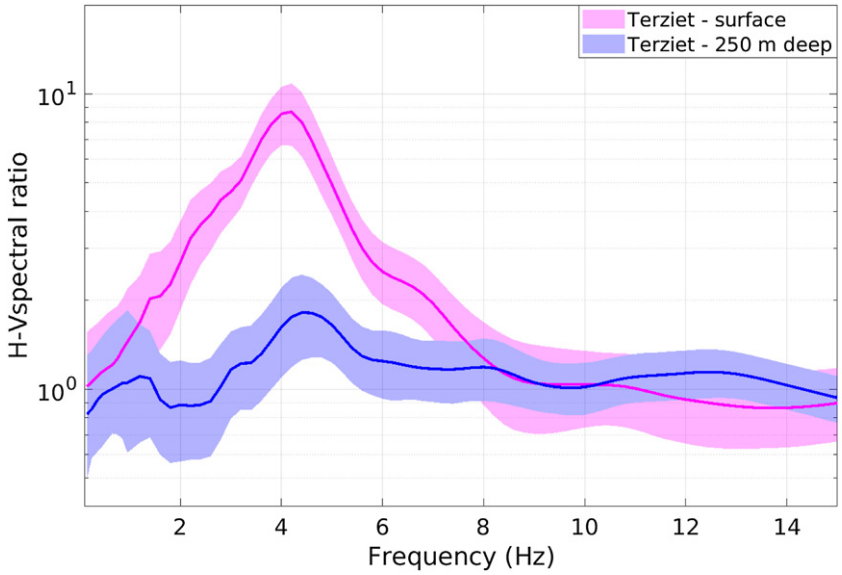

Figure 8. Ratio of horizontal and vertical PSDs at the surface and 250 m underground at the borehole location in Terziet. The surface ratio strongly peaks at about 4 Hz.

the horizontal amplitudes significantly exceed vertical amplitudes on the surface at high frequency. The maximum ratio on the surface is reached at about 4 Hz, and such a high frequency peak is characteristic for a soft-soil layer on hard-rock geology [49]. For increasing depth and frequency, the surface amplitudes are attenuated more efficiently and the ratio approaches a nearly constant level across all frequencies.

In summary, the geophysical studies at the EMR candidate site in Terziet, Limburg, resulted in the identification of five distinct subsurface layers. The geology of the site is characterized

by a soft-soil formation on the surface of about 35 m thickness, resting on hard-rock material of which the deepest layer starts at a depth of about 90 m. The studies allowed to derive the thickness and density of the five subsurface layers, their P- and S-wave speeds as well as the surface-wave speeds of fundamental and first overtone. Together with PSD measurements on the surface, the mostly local seismic noise sources were determined for frequencies from 2.4 to 14.0 Hz. Tri-axial, simultaneous measurements of ambient seismic noise on the surface and at 250 m depth demonstrate a strong reduction of underground PSDs with respect to those at the surface. Moreover, these measurements allow to infer the presence of a significant body-wave background at frequencies above about 4 Hz, and allow the identification of a site-characteristic $H-V$ spectral ratio. The surface and underground PSD measurements reveal diurnal and annual variations [30].

3. Modeling the ambient seismic displacement field

The behavior of soil under dynamic loading conditions is typically complex, an-isotropic, and nonlinear. If the forces that excite a soil profile are small, then it can be assumed that the soil behaves like an elastodynamic medium. The theory of elasticity [47, 50] is a major building block of seismology, as it uses concepts known from classical mechanics such as stress and strain to derive the propagation of seismic waves through solids such as rock. External forces on the medium lead to displacement and deformation and hence stress and strain are inevitably linked to each other through the elasticity tensor. For an isotropic medium this tensor can be expressed in terms of the so called Lamé parameters μ and λ, which are defined as

$$\mu \equiv \frac{E}{2(1+\nu)}, \qquad \lambda \equiv \frac{E\nu}{(1+\nu)(1-2\nu)}, \tag{3.1}$$

where E represents the Young's modulus and ν the Poisson ratio. Making use of the relation between stress and strain allows to express the displacement field $\vec{u}(\vec{x}, t)$ as

$$(\lambda+\mu)\nabla\left(\nabla\cdot\vec{u}\right)+\mu\nabla^2\vec{u}=\rho\frac{\partial^2\vec{u}}{\partial t^2}, \tag{3.2}$$

where ρ represents the density, $\vec{x}$ the position vector and t time.

We model the ambient seismic displacement field by solving the elastodynamic wave equation (3.2) [51] for the geology model shown in table 1 that has been derived from active and passive seismic sensor-array studies. This expression shows the elastodynamic wave equation for the displacement field. Equation (3.2) is solved in the frequency domain by using the direct-stiffness matrix method [52]. A uniform damping factor of 1% was chosen for all layers as it is representative for the high damping values found in clay structures and the low damping of rock formations [53]. We employed damping ratios that were similar to ones we obtained from ambient seismic noise analysis at the Virgo site [31]. At Virgo, we found a damping factor of about 1.3% corresponding to soft soil and about 0.6% corresponding to hard rock. The damping for P- and S-waves is taken into account by adding an imaginary component to the Lamé parameters.

Figure 9 shows the result of a simulation of the displacement noise at the EMR-site at 2.6 Hz. In the simulation the surface has been excited by 180 vertical sources, which are distributed uniformly in a 240 m wide ring of radius $R \approx 1$ km. The distance R is selected to reproduce the $H-V$ ratio measured at the borehole location. In addition, the source locations are required to be compatible with the directions derived from beamforming of Array A data.

With 180 excitation points, each of the sources is located in a segment of 2° width. The relative strength of the sources is selected to reproduce the beampower measured with Array A.

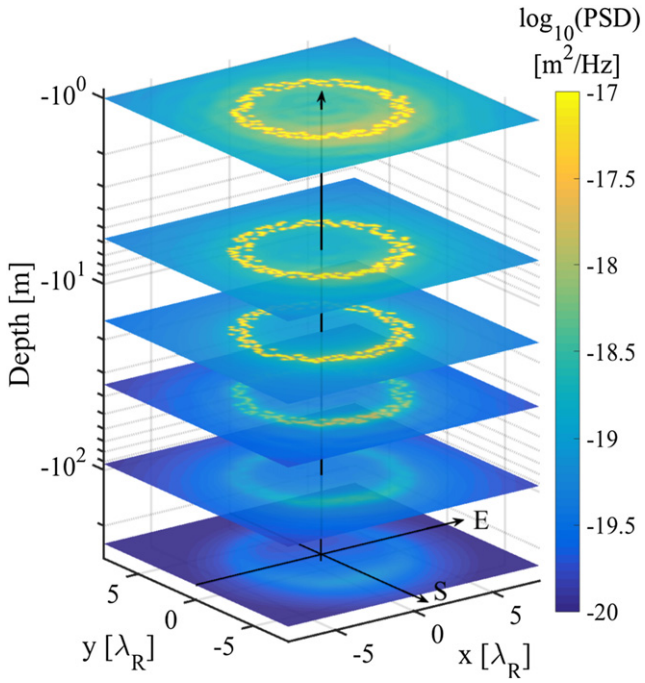

Figure 9. Model of displacement noise that reproduces the measured PSD at 2.6 Hz on the surface at the borehole. The first five sheets show the PSD across the top of each new subsurface layer. The sheet at 250 m depth shows the PSD near the test mass. Note the strong amplitude reduction at depths greater than 35 m, where the transition to hard-rock layers begins.

Due to the topography of the array, beampower values are available only for frequencies from 2.4 to 14 Hz, while the Newtonian-noise frequency band of interest is from 1 to 20 Hz. Hence, for frequencies smaller than 2.4 Hz the same beampower distribution in azimuthal angle as for 2.4 Hz is assumed, whereas for frequencies larger than 14 Hz a uniform distribution is assumed. The absolute scaling factor is derived from the vertical PSD of the surface seismometer at the location of the borehole. Next, as a consistency check, we compare the results obtained with our solution to the wave equation to the results of our measurements.

3.1. Surface horizontal over vertical PSD spectral ratio

The PSDs of the horizontal and vertical components of the displacement field detected by a receiver depend on the distance between this receiver and the source of the seismic field. To approximate the situation at the site, we require our model to reproduce the H/V ratio measured on the surface. In our model we only used sources that excite the earth in vertical direction for the following reasons: firstly our surveys were performed with vertical sensors (and for the active survey, with vertical sources) and hence we believe that we are more sensitive to the vertical PSD ratio's. Secondly, vertical sources in a horizontally layered medium will spread radially outwards, whereas horizontal sources will produce different displacement amplitudes in different directions. Therefore, the use of horizontal sources would complicate the interpretation of our simulation results and introduce an extra degree of freedom (the location and the direction of excitation). Since vertical sources are perfectly capable of exciting the dominant

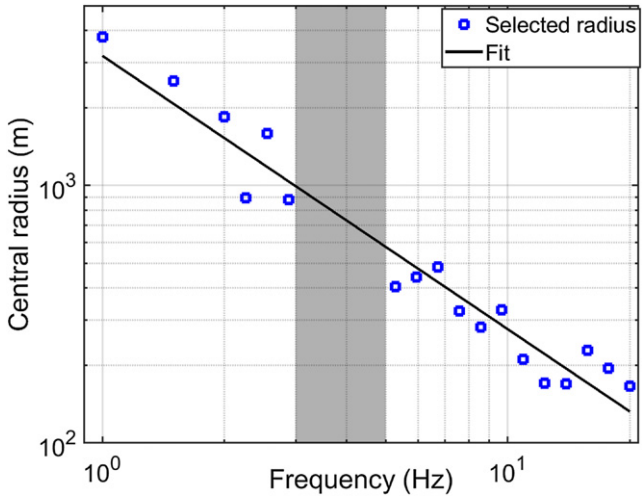

Figure 10. Central radii of the source ring as a function of excitation frequency. For each frequency, the radius has been chosen such that the $H-V$ ratio of a single source reproduces the measurement at the center of the ring.

Rayleigh waves (which exhibit elliptical polarization, so at some distance from the source the horizontal PSD will attain sufficient strength) we opted for using only vertical sources with consequently symmetrical displacements in the horizontal plane. We assume that far away from the source, after rescattering and dispersive effects, the excitation direction of the source will be irrelevant, i.e. that vertical sources can sufficiently excite the horizontal displacement field. Finally, for the *surface* term in the expression for Newtonian noise (see equation (4.4)), only vertical displacements (normal to the surface) contribute. Figure 10 shows the source distances R that correctly predict the $H-V$ ratio measured with the T240 surface sensor near the top of the borehole. This means that for low frequencies the sources may be several km away, whereas at high frequencies the sources are local and may be a few hundreds of meters from the test mass.

For most frequencies in the range of interest, that is from 1 to 20 Hz, a source distance can be determined. However, between about 3 and 5 Hz the measured $H-V$ ratio cannot be reached. This deviation indicates that the soil model that is used at the location of the borehole sensor may not be exactly the same as the soil model derived at the center of Array A. Even though borehole and the array's center only lie about 300 m apart, the area is known to exhibit changes in the thickness of the soft-soil layer [30]. Alternatively, it may mean that the source mechanism is important; i.e. horizontal sources are needed in this frequency band to describe the local spectrum. The radius in the frequency band from 3 to 5 Hz is derived from the fit in figure 10.

3.2. Beamforming and dispersion curve

The energy distribution between the fundamental and higher-order modes depends on many factors: material properties such as wave speeds and attenuation factors of the layers, source mechanism and distance between source and receiver [48]. Beamforming of synthetic data is used as an independent method to verify if the derived soil model and source distribution are a good approximation of the actual situation at the site.

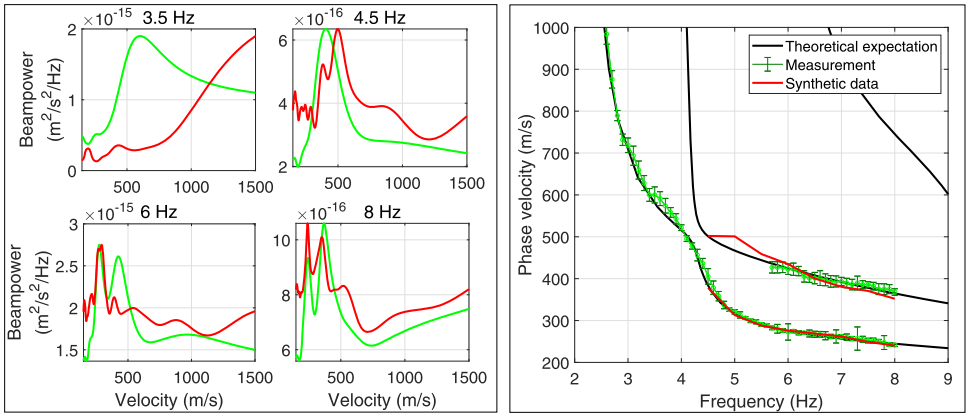

Figure 11. Left: surface-wave speed and corresponding beampower derived from site measurements (green) and synthetic data (red) for representative frequencies. Above 4.5 Hz the results of beamforming of measured and synthetic data are in fair agreement, while for lower frequencies uncertainties in the geology model lead to deviations. Right: the fundamental-mode and first-overtone dispersion curves that have been derived from beamforming of measured and synthetic data are in good agreement and follow the dispersion curves predicted by the soil model. The error-bars in the measurements correspond to one standard deviation.

Synthetic data were derived by exciting the soil with a ring of vertical sources as described in the previous section. Beamforming and dispersion curve data are available from Array A for frequencies from 2.4 to 14 Hz. As the data from the sensor array only encompass vertical displacements, the beamforming analysis was carried out on the vertical synthetic data.

Figure 11, left panel, shows that beamforming of synthetic data allows to reproduce the general features of the measured source distribution for frequencies above 4.5 Hz. The surface-wave velocity shows two peaks that can be attributed to the fundamental mode and the first overtone. In the modeled data the first overtone is visible already above 4 Hz. However, the energy distribution between fundamental and higher-order mode deviates from the measured values. This deviation can be attributed to unknown material damping ratios in the model and to the uncertainty in the source distance. Below 4.5 Hz the beampower peak is not well recovered from the synthetic data, which may be attributed to uncertainties in the geology model for this frequency range.

The dispersion curve (figure 11, right panel) can be obtained by selecting the velocities corresponding to the beampower peaks at each individual frequency. Fundamental mode and first overtone are recovered and are in good agreement with the theoretical expectation of the soil model. Deviations below 5 Hz in the overtone are again attributed to uncertainties in the geology model. Since the limitations of the model only encompass a small part of the frequency range of interest for Newtonian noise, it can be concluded that the model and the applied source distribution are a fair approximation of the actual situation at the site. In summary, we have derived a layered model that is in reasonable agreement with the measured angular and beampower distribution of seismic sources, the fundamental-mode and the first-overtone dispersion curve, and the $H-V$ spectral ratio.

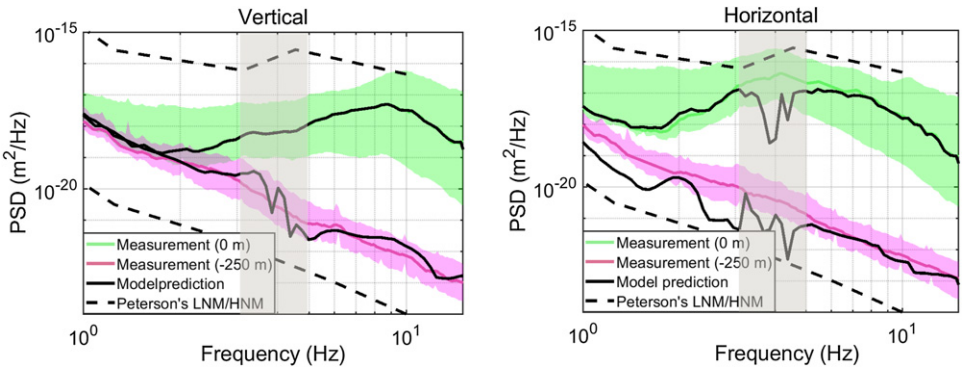

Figure 12. Mean of vertical (left panel) and horizontal (right panel) displacement PSD of synthetic data in comparison to surface and subsurface data of the borehole seismometers. The shaded bands enclose the 10th and 90th percentiles. The source strength has been set for the simulated vertical surface PSD to reproduce the measured PSD. The model predicts surface and subsurface PSDs that are in fair agreement with the measurements, except between 3 and 5 Hz (shaded gray).

3.3. Surface and underground ambient displacement noise

With the source distribution obtained in the previous section, an ambient seismic field is derived. While the relative strength of each source is set to reproduce the measured beamforming profile, the absolute source strength in the model is set by scaling the vertical PSD of the synthetic data to that of the surface sensor at the borehole. The model then allows to predict the horizontal PSD on the surface as well as the underground PSDs for horizontal and vertical direction at 250 m depth.

Figure 12, left panel, shows that the simulated vertical underground PSD is in good agreement with the data. The model correctly predicts the characteristic large attenuation in power of surface waves. The simulated horizontal surface spectrum is in excellent agreement with the measured data except for frequencies from about 3 to 5 Hz (indicated by the shaded gray vertical band), where the model predicts lower horizontal PSDs. The simulated horizontal underground PSD is in good agreement with the measured data for frequencies above 5 Hz. Again, deviations are seen between 3 and 5 Hz and moreover the model exhibits a significant deviation from the measured data below 3 Hz. We attribute these anomalies to uncertainties in the geology model. This assumption is supported by the results from our active seismic-array studies [30], that identified an underground fault and a fast variation in the thickness of the soft-soil layer. This indicates that the horizontally-layered subsurface composition at the center of the sensor array is only to first-order representative for the lithology at the borehole.

Ambient seismic noise in the frequency band of interest for Einstein Telescope can be created by sources at the surface. For the EMR-site anthropogenic noise is a main consideration due to the vicinity of cities like Aachen, Maastricht, and Liège. Ambient noise excitation at the surface leads to the creation of Rayleigh and Love waves. Rayleigh waves are low-frequency waves with significant energy, while Love waves are horizontally-polarized surface waves. Both surface waves propagate strongly dispersive and decay exponentially with depth. These surface excitations will also create body waves such as P- and S-waves that propagate nearly non-dispersively outward from the source with expanding quasi-spherical wave fronts. At the location of an underground detector these ambient surface and body waves will be present and

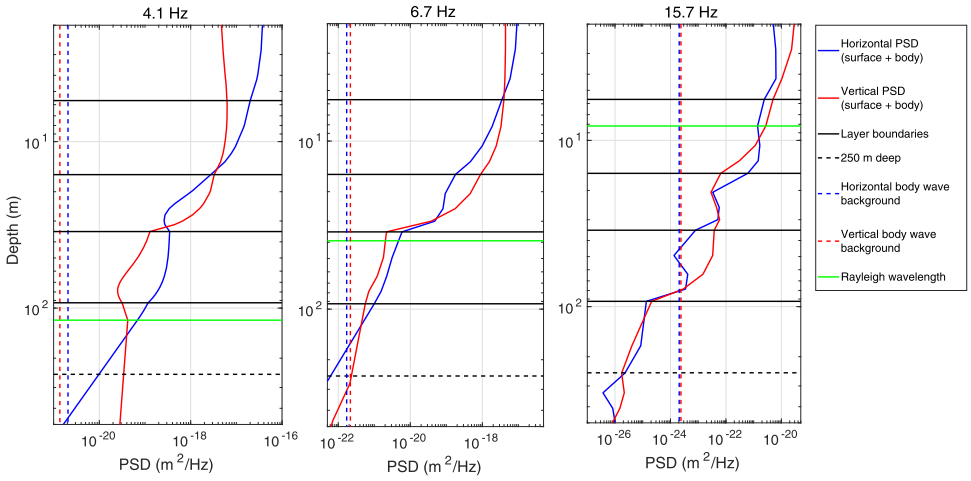

Figure 13. Depth profile of horizontal (blue) and vertical (red) displacement PSD for representative frequencies. The subsurface layers are indicated by solid-black horizontal lines. The Rayleigh wavelength is based on the dispersion curve and shown by the green horizontal line. The depth of the test mass is indicated with a dashed-black line. At all frequencies, the displacement noise PSD ratio between surface and at the depth of the test mass is several orders of magnitude. The energy of the surface waves is mostly confined to the shallow subsurface layers.

affect the instruments through seismic and Newtonian noise. Therefore it is important that the power in these waves is sufficiently attenuated at 250 m depth when reaching the optical elements of Einstein Telescope. Figure 13 shows that our model predicts a strong attenuation in surface-wave power for the EMR-site. Moreover, the results of borehole measurements shown in figure 12 confirm the validity of our model.

We observe that the vast majority of Rayleigh-wave power does not reach the borehole seismometer. However, this sensor measures a combination of residual surface-wave noise and a random body-wave background noise. This body-wave background is a superposition of body waves with random angles of incidence that arrive from unknown and relatively far-away surface and underground sources. The origin of this background may be related to crustal phases [54] and distant earthquakes. We have quantified the random body-wave by investigating the temporal variation of surface and underground PSDs [30] and the results are shown as dashed vertical lines in figure 13. We observe that the body-wave background is negligible at the surface, but dominates the displacement PSD at 250 m depth for frequencies above about 5 Hz (see middle panel in figure 13). The presence of the random body-wave background indicates that, from the viewpoint of Newtonian noise, there is no advantage of building Einstein Telescope at much greater depth than 250 m. However, one must be cautious about hosting Einstein Telescope less deep (generalizing Terziet conditions). Decreasing the depth not only leads to an increase of the local PSD at the mirror, but also the distance to the surface-layers is decreased: for identical surface-layer seismic-noise PSD, the surface contribution to Newtonian noise will be 6 times higher when the depth of the observatory is reduced by a factor of 2.5.

4. Newtonian noise

4.1. Introduction

Modeling Newtonian noise requires a description of the local seismic field and geology. The first estimates for Newtonian noise have been derived by Weiss and Saulson [17, 18,] and Saulson's approach is used until today for Newtonian-noise estimates in the design sensitivity of gravitational-wave detectors [12, 55]. Since numerical solving tools were not available at that time, Saulson based his model on an analytical derivation assuming a detector on the surface and a half-space geology with density ρ. Furthermore, it is assumed that the seismic field consists of independent regions that are coherent across a length of $\lambda/2$, where λ represents the seismic wavelength. It is assumed that these regions fluctuate independently of each other, and that the Newtonian acceleration of the test mass can be formulated as an incoherent sum over the contributions from the individual patches. The horizontal component of the Newtonian acceleration, i.e. parallel to the detector arm in the x_1-direction, is then derived as

$$|\delta\ a_1(f)|^2 = \sum_i \left|\frac{F_{i,1}}{M}\right|^2 = G^2 \sum_i |\Delta m_i(f)|^2 \frac{\cos^2\theta_i}{|\vec{r}_i|^4}, \tag{4.1}$$

where $F_{i,1}$ represents the horizontal component of the force between the test mass with mass M and the mass fluctuation Δm_i of the i^{th} volume element at location $\vec{r}_i$, θ_i the angle between the volume element and the detector arm, f the frequency and G the gravitational constant. To facilitate the sum, it is converted to an integral where a lower cutoff radius of $\lambda/4$ is introduced to avoid a singularity as $|\vec{r}_i|$ approaches zero. Next, it is assumed that the fluctuation of mass $\Delta m_i(f)$ in the volume element is directly proportional to the displacement amplitude $\Delta X(f)$ of the coherent region, which is in units $(\mathrm{m}\sqrt{\mathrm{Hz}}^{-1})$ and a quantity that is measurable by seismometers. For simplicity it is assumed that the amplitude of the displacement is uniform across the entire half-space surrounding the test mass. The expression for the horizontal displacement Newtonian noise $|\delta x_1(f)|^2$ of four independent test masses was derived as

$$|\delta x_1(f)|^2 = \frac{|\delta a_1(f)|^2}{(2\pi f)^4} = \frac{16\pi^2}{3}\frac{G^2\rho^2}{(2\pi f)^4}|\Delta X(f)|^2\ (\mathrm{m^2\,Hz^{-1}}). \tag{4.2}$$

It is important to understand that Saulson's result in equation (4.2) is only valid for a surface detector where the integration is carried out over a half-space, and where no explicit assumptions have been made on cavern shape, geology, source distribution, seismic wave types, possible mode conversions, damping and amplitude attenuation with distance or depth. Moreover, it needs to be understood that the cutoff condition of $\lambda/4$ applied by Saulson, leads to the factor $16\pi^2/3$ in equation (4.2); this factor is inversely proportional to the cutoff radius $r_{\min}$.

The size of the coherent region enters in Saulson's result, with a second power for surface contributions. This is important when one would estimate the contribution from the surface waves; they do not scale with $|\Delta X|^2$, but with $|\Delta X|^2\lambda^2$, assuming that the coherent region scales linearly with λ and one uses a fixed cut-off radius or mirror depth. This dependence on wavelength is hidden in the expression for Δm_i and in the cut-off radius in Saulson's model and is easily overlooked; a site with half the wave speed for surface waves exhibits four times lower Newtonian noise, assuming that the contribution from displacements in the surface layers dominates; the Newtonian noise from body waves for an underground mirror scales only linearly with wavelength, assuming a fixed cut-off radius around the mirror.

In an attempt to overcome some of the simplifications in the wavefield, the analytical model has been expanded by assuming plane Rayleigh waves, contributions from bulk and surface

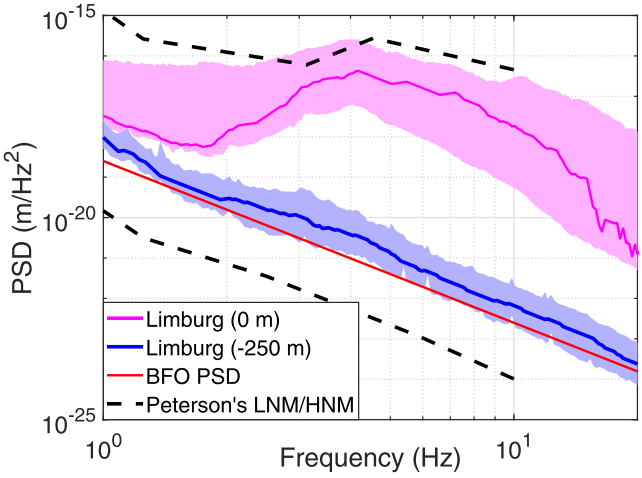

Figure 14. Horizontal PSD at the surface and at 250 m depth measured at Terziet in Limburg in comparison to the 10th percentile of the PSD measured underground during night-time at 95 m depth at the Black Forest Observatory. The BFO PSD was used to predict the Newtonian noise for the ET-D Einstein Telescope sensitivity, and is compatible with the 10th percentile of the underground PSD in Limburg.

of a half-space and dispersive soil properties [21–23]. Combining these methods leads to an expression for the horizontal displacement Newtonian noise of a surface detector as [20]

$$|\delta x_1(f)|^2 = 4\pi^2\beta^2\frac{G^2\rho^2}{(2\pi f)^4}|\Delta X(f)|^2 e^{-\frac{2\pi h}{\lambda}}, \tag{4.3}$$

where h represents the height of the test mass above ground and the factor $\beta < 1$ is related to the dispersive properties of the site's geology. For the geology at the LIGO detectors, β has been estimated to be of the order $\beta \approx 0.35$–0.6 for quiet and $\beta \approx 0.15$–1.4 for noisy times [23].

This model has been used for Newtonian-noise estimates in the Advanced Virgo design sensitivity curve [55, 56] and in the conceptual design study for Einstein Telescope. The Einstein Telescope design sensitivity (so called ET-D) contains a Newtonian-noise contribution that has been derived from equation (4.3), where $\beta = 0.58$, $\rho = 2{,}500\,\mathrm{kg\,m^{-3}}$ and where the exponential term containing the test mass height has been omitted [12]. This model has been derived for a surface detector that is surrounded by a half-spherical cavern of a frequency-dependent radius of $\lambda/4$, where λ represents the wavelength of the constant seismic field. Even though this model does not apply for an underground detector, it has been used to generate the Einstein Telescope sensitivity curve [12, 57]. Moreover, scientific papers have been written with event rates based on this Einstein Telescope sensitivity, see [13] and references therein.

Figure 14 shows the seismic displacement that has been used in the ET-D estimate of Newtonian noise. It amounts to $5 \times 10^{-10}\ \mathrm{f}^{-2}\ \sqrt{\mathrm{Hz}}^{-1}$ and corresponds to a fit of the 10th percentile of the ambient seismic noise spectrum measured during night-time at 95 m depth at the Black Forest underground observatory (BFO) in Germany [57, 58].

The models on which ET-D was based were restricted to surface waves, since no detailed geological model of the subsurface at the detector sites nor a realistic distribution of noise

sources and their spectral content was at hand [12, 57, 59]. Together with finite-element models of underground seismic fields in homogeneous media [15, 26], early studies stressed the necessity of a detailed seismic model.

4.2. Toward an estimate of site-based Newtonian noise at Terziet in Limburg

We derived an ambient seismic displacement field that is based on solving the elastodynamic wave equation for parameters and boundary conditions that are specific for the site at Terziet in Limburg. We employ a five-layer horizontally-stratified geology based on results of passive and active seismic-array studies. A realistic source distribution is used that reproduces measured beamforming and $H-V$ spectral ratios, and which is normalized to the vertical surface-displacement PSD at the borehole location. First we discuss the calculation of Newtonian noise due to this surface-source distribution. The ambient body-wave background, that contributes to the Newtonian noise at higher frequency, is discussed in Section 4.5.

For a test mass located at a depth h, the Newtonian acceleration in a horizontally layered medium with M layers, can be expressed as

$$\delta\vec{a}(f) = \sum_{m=1}^{M} G\left(\int_V \rho_m\,(\vec{u}\cdot\nabla)\,\vec{k}\,\mathrm{d}V_m + (\rho_{m-1}-\rho_m)\int_S (\vec{u}\cdot\hat{n}_m)\,\vec{k}\,\mathrm{d}S_m\right), \tag{4.4}$$

where the volume and surface integral of the m^{th} layer are represented by $\mathrm{d}V_m$ and $\mathrm{d}S_m$, and the vector normal to the horizontal interface of the m^{th} layer is indicated with $\hat{n}_m$; $\vec{k}$ is defined as $\frac{\vec{x}}{|\vec{x}|^3}$. The 3D displacement field is given by $\vec{u}(\vec{x},f) = (u_1(\vec{x},f), u_2(\vec{x},f), u_3(\vec{x},f))$, the density of each layer is indicated with ρ_m. The Newtonian acceleration of a test mass due to the seismic field from N incoherent sources is calculated by first deriving the Newtonian noise for the complex displacement field of each source individually, followed by summing these contributions incoherently. The contribution of Newtonian noise to the output of a gravitational-wave detector is due to the seismically-induced Newtonian acceleration at all four test masses. We assume that for a detector with distance L between the test masses, the interferometer arms are typically much longer than the seismic wavelengths for frequencies above 2 Hz. This implies that the forces on the test masses are uncorrelated and the total Newtonian-noise PSD is obtained by a sum over the contributions of the individual test masses. Note that only the horizontal test mass motion parallel to the detector arms enters the calculation of Newtonian noise.

Previous studies relied on carrying out the Newtonian-noise integral in terms of finite-element modeling in homogeneous media [15, 22, 26]. The finite-element modeling approach has strict conditions in terms of grid symmetry and requires a dense spacing between the volume elements in the grid in order to calculate Newtonian noise to the required precision. Although that approach may still be feasible for surface detectors, where the largest wavelength to consider is the Rayleigh wavelength, for underground detectors like Einstein Telescope much larger integration areas have to be considered and an evaluation of the integral via finite-element modeling is computationally challenging. Compared to previous studies [22, 26], this work computes the integral with Gaussian quadrature, a numerical integration method where the integrand is approximated at n points by a set of orthonormal (in our case Legendre) polynomials. The numerical approximation of the integral is exact up to order $2n-1$ in the polynomial expansion of the integrand [60]. This approach yields high accuracy and presents an improvement in computation time of several orders of magnitude.

Einstein Telescope will be located underground at a depth between 100 and 300 m [12]. As the final depth is not defined yet, a detector location of 250 m underground, equivalent to the depth of the borehole seismometer, has been chosen for the present analysis. To approximate the effect of a spherical cavern around the test mass, a minimum value for the integration radius of 10 m is used. Next, we discuss the choice of the maximum integration radius for the integrals in equation (4.4).

4.3. Integration radius for surface sources

The maximum integration radius $r_{\mathrm{NN}}^{\mathrm{max}}$ is the distance after which Newtonian noise does not significantly change when the integration volume is increased any further. Previous studies in homogeneous half-space geologies with Rayleigh waves and surface detectors have shown that an integration radius of $r_{\mathrm{NN}}^{\mathrm{max}} \approx \lambda_{\mathrm{R}}/2$ is sufficient to reach a stable Newtonian-noise PSD within about 10% [26]. This generalization is not evident for test masses in layered geologies with realistic wave fields and for underground caverns. Therefore we derived $r_{\mathrm{NN}}^{\mathrm{max}}$ for a test mass at 250 m depth, with a spherical cavern of radius 10 m in the Limburg geology. The $r_{\mathrm{NN}}^{\mathrm{max}}$ in each frequency bin is determined from the contribution of a single source by subsequently increasing the integration radius, starting with 250 m and reaching up to a distance where fluctuations stay within 10% of the asymptotic value.

The maximum integration radius $r_{\mathrm{NN}}^{\mathrm{max}}$ for each frequency bin for a test mass at 250 m depth is displayed in figure 15. The $r_{\mathrm{NN}}^{\mathrm{max}}$ exceeds λ_{R} across the full frequency band by at least one order of magnitude and is always larger than 250 m. This means that at all frequencies the seismic surface displacements are included in the calculation of the underground Newtonian noise, even though the Rayleigh wavelengths may be much shorter than the distance between surface and test mass. Note, that $r_{\mathrm{NN}}^{\mathrm{max}}$ surpasses the central radius of the source ring (indicated by the dashed curve in figure 15), which means that sources are included in the integration volume. This is a reasonable assumption and supported by the beamforming analysis showing that the noise sources are very local and in close vicinity of the sensor array. Increasing the source distances to remove them from the Newtonian-noise integration area is in principle possible, but will not allow to reproduce the measured H–V ratio at the central part of the model, which is in turn required to reproduce the measured PSDs near the test mass. Also, placing the surface sources very far away will decrease the numerical accuracy and increase the computational time of the elastodynamic calculations, that consider all paths between source and soil integration point.

Newtonian noise is derived from the incoherent sum of the contributions of the individual surface sources where each individual numerical integral is approximated by a weighted sum over a discrete number of points within the integration volume [32]. Less than 2% of these discrete points are within a radius $\lambda_{\mathrm{R}}/2$ from the source. To avoid a bias due to the excess displacement in the vicinity of the source, all seismic displacements within $\lambda_{\mathrm{R}}/2$ are excluded. If a discrete integration point is located in this area, then its displacement is determined by a linear interpolation based on the displacement field outside the excluded source area.

For surface excitations, the Newtonian-noise contribution from each individual layer to the total Newtonian noise is frequency dependent. At low frequencies, Newtonian noise from the bottom-most layer, in which the test mass is located, is dominant. At these frequencies the wavelengths of the Rayleigh waves are of the order of 1 km and their amplitudes dominate the wave field, even at the depth of the test mass. As the frequency increases, the Rayleigh-wave amplitudes attenuate faster with depth and become less important for the wave field at the test mass. Thus the contribution of the bottom-most layer to the Newtonian noise gradually decreases. For frequencies above about 5 Hz Rayleigh waves are strongly attenuated when they reach the location of the test mass. The wave field near the test mass will then have a

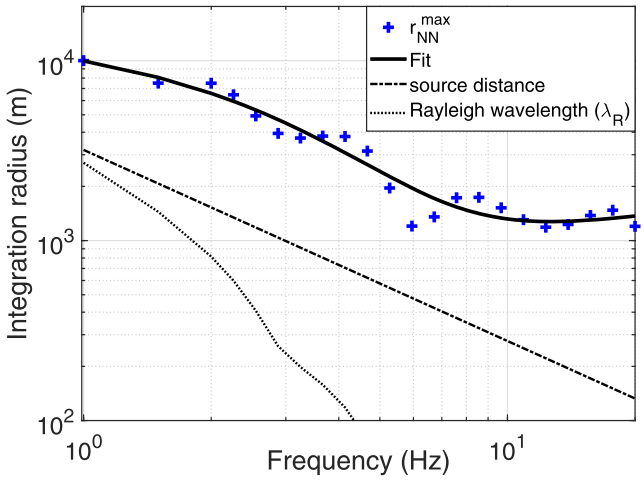

Figure 15. Frequency dependence of the maximum integration radius $r_{\mathrm{NN}}^{\mathrm{max}}$ for a test mass located at 250 m depth in the Limburg geology. The $r_{\mathrm{NN}}^{\mathrm{max}}$ exceeds the central radius of the source ring (dashed curve), which means that surface sources are included within the integration volume. The Rayleigh wavelength is indicated by the dotted curve.

contribution from a random body-wave background that will become increasingly important with increasing frequency. We will discuss in Section 4.5 that this background of body waves, with random angles of incidence, is expected to constitute the dominant source of Newtonian noise.

4.4. Newtonian noise from surface excitations

Newtonian noise for Einstein Telescope at the EMR-site in Limburg is estimated for a realistic, horizontally-layered geology that is excited with 180 vertical seismic noise sources, as described in Section 3. The sources are placed on the surface; the simulated ambient seismic field reproduces the beam power as well as the surface and underground PSDs that have been measured during the field studies described in the introduction of Section 2. The Newtonian noise from surface sources has been calculated according to equation (4.4), where Gaussian quadrature is used to perform the numerical integrals. The residual contributions from body-waves is discussed in the next section. The test mass was placed at a depth of 250 m underground and surrounded by a spherical cavern of radius 10 m.

Figure 16 gives the prediction for Newtonian noise in Limburg from simulated seismic displacements of the entire subsurface, including the free surface, and modeled with surface sources. The mean (solid-green curve) of the contribution from surface excitations is compatible with the ET-D Einstein Telescope sensitivity curve as defined in [12, 57]. From the viewpoint of Newtonian noise generated at the surface, the EMR-site offers suitable conditions to host Einstein Telescope. Moreover the predicted contribution from surface excitations is well below the Newtonian-noise projection that is presented in the recent update of the Einstein Telescope design report [59]. At frequencies below 3 Hz the site-based Newtonian noise of the 90th percentile is predicted to be approximately equal to the Einstein Telescope design sensitivity curve. Here, Rayleigh wavelengths are large and the seismic waves in the bottom-most layer give the dominant contribution to Newtonian-noise estimates. The dip just before 3 Hz is an artifact of the underestimated horizontal underground displacement in the seismic

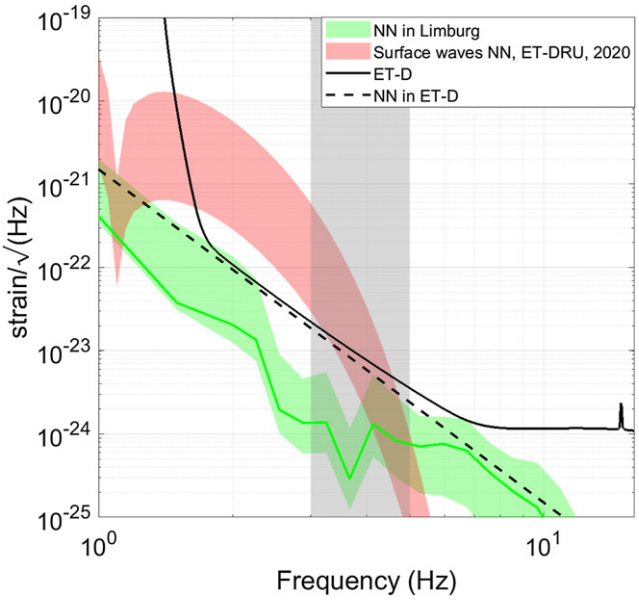

Figure 16. Estimate of Newtonian noise from surface sources at the EMR-site for test masses at 250 m depth enclosed in 10 m radius caverns. The mean (solid-green curve) is compatible with the ET-D sensitivity (solid-black curve) of which the Newtonian-noise contribution is shown by the dashed-black curve. The red band shows the projection of surface-wave Newtonian noise in the 2020-update of the Einstein Telescope design report [59]. The vertical gray band indicates the region with significant uncertainty in the geological model.

model at low frequencies (see figure 12). In the band from 3 Hz to 5 Hz, seismic amplitudes are uncertain due to the limitations in the geology model and as a result the Newtonian noise in this area can be considered a lower limit. At frequencies above about 5 Hz, surface waves in the top layers are the main contributor to the total Newtonian-noise level. Their wavelength decreases with increasing frequency, and thus the ratio of test mass depth and wavelength increases. As a result the surface-generated Newtonian noise decreases strongly with increasing frequency.

Note that even though the 10th percentile of the underground PSD at the EMR-site is compatible with the BFO PSD (see figure 14), the 10th percentile of the site-based Newtonian noise is about one order of magnitude below the Newtonian noise of the Einstein Telescope sensitivity [12, 57], and more than two orders of magnitude below the expectation in the updated Einstein Telescope design report [59]. This is mainly due to the small wavelengths at the surface and the strong attenuation with depth, characteristic for the layered geology at the EMR-site. This shows that it is insufficient to only consider PSDs in a comparison between candidate sites for Einstein Telescope, but that one must derive Newtonian-noise estimates that take into consideration the geological and seismic conditions that are characteristic for the candidate site, and especially the wavelengths of surface waves.

4.5. Newtonian noise from a random body-wave background

The modeling described in the previous section was concerned with estimating the contribution to Newtonian noise from surface excitations. By solving the wave equation for the geology at Terziet, we derived a wave equation that reproduces the measured surface PSD. As described

in [30] and mentioned in the previous sections, part of the spectrum underground is due to body waves, a constant background created by (possibly underground) far-away sources. We lack detailed knowledge to fully characterize the spectrum of these body waves as this would require data from an underground sensor network, where the body-wave contribution dominates and can be separated from the surface-wave contribution. Instead, we used the result of [30], where the strength of the body-wave content was fitted by inspecting the day–night variation in the horizontal and vertical PSDs at the surface and in the borehole, under the assumption that the body-wave background is constant in power during day and night. In order to model the displacement field $\vec{u}$ resulting from body waves, we assume plane waves

$$\vec{u}(\vec{x}) = (\vec{A}\cdot\hat{\xi})\hat{\xi}\,\mathrm{e}^{-\mathrm{i}(\frac{\hat{\xi}\cdot\vec{x}}{v_\mathrm{P}}-\omega t)} + (\vec{A}-(\vec{A}\cdot\hat{\xi})\hat{\xi})\mathrm{e}^{-\mathrm{i}(\frac{\hat{\xi}\cdot\vec{x}}{v_\mathrm{S}}-\omega t)} \tag{4.5}$$

with $\vec{A}$ the amplitude and direction of the displacement, $\hat{\xi}$ the unit vector pointing in the direction of the wave, $\vec{x}$ the soil coordinates, and v_P (v_S) the P-wave (S-wave) speed. Both the displacement amplitude $\vec{A}$ and the wave direction $\hat{\xi}$ are assumed to be distributed isotropically. This implies that the displacement power spectral densities consist of 1/3 P-waves ($\vec{A}$ parallel to $\vec{\xi}$) and 2/3 S-wave components ($\vec{A}$ perpendicular to $\vec{\xi}$). We use fixed wave speeds for all frequencies, 4.50 km s^{-1} for P-waves and 2.82 km s^{-1} for S-waves. Furthermore we assume random phase offsets for each component (sideways, parallel, perpendicular). More realistic modeling of body waves requires solving the elastodynamic equations for underground sources, as well as obtaining measurements of the displacement field at various depths to calibrate the models, and is beyond the scope of the current work.

The assumption of plane waves implies that we do not consider rescattering and dispersion of the waves; the waves are not modified when crossing a soil layer boundary and the amplitude is constant everywhere in space; the coherence length is infinite. Therefore we expect that the modeled results for the body waves may overestimate the Newtonian noise. Note that both P- and S-waves contribute to the Newtonian noise via the term $\vec{u}\cdot\nabla\vec{k}$ in equation (4.4); only in very special cases can the S-wave contributions be ignored. In a homogeneous volume P-waves introduce density gradients in the direction of the wave whereas S-waves introduce deformations perpendicular to the wave direction. For a homogeneous finite spherical mass distribution, both wave types generate accelerations aligned with the direction of the displacement, and for non-spherical distributions, such as in our case the vertical direction, the surface boundaries can contribute in complicated ways. Since we have no knowledge of the angular distribution of the body-wave background at the Limburg site, we assume isotropic contributions and we calculate the Newtonian noise for the P- and S-wave components separately. This allows to inspect the relative importance of these different components of the spectrum.

The body-wave background is modeled with 4000 isotropically-distributed plane waves at each frequency, of which the total power matches the deduced body-wave PSD. In the Newtonian noise calculations, the soil displacements due to these waves have been integrated up to a radius of 10 km. Figure 17 shows the Newtonian noise from body waves, along with the ET-D design sensitivity, scaled to the mean PSD for body waves as derived in [30]. Also the partial contributions from P- and S-waves are shown; the P-wave contributions are about 10% higher for frequencies below 2 Hz to maximally 40% higher around 6 Hz than that of the S-waves. Our choice of taking an isotropic mixture of 1/3 P-wave and 2/3 S-waves may thus result in a slight under-prediction; in the most extreme case, if we assume 100% P-waves at 6 Hz, the predicted Newtonian noise would be larger by a factor of 1.4 in our model.

The contributions to the Newtonian noise from the layer boundaries (most notably the boundary at the surface) are also shown in figure 17. This is the contribution from mass

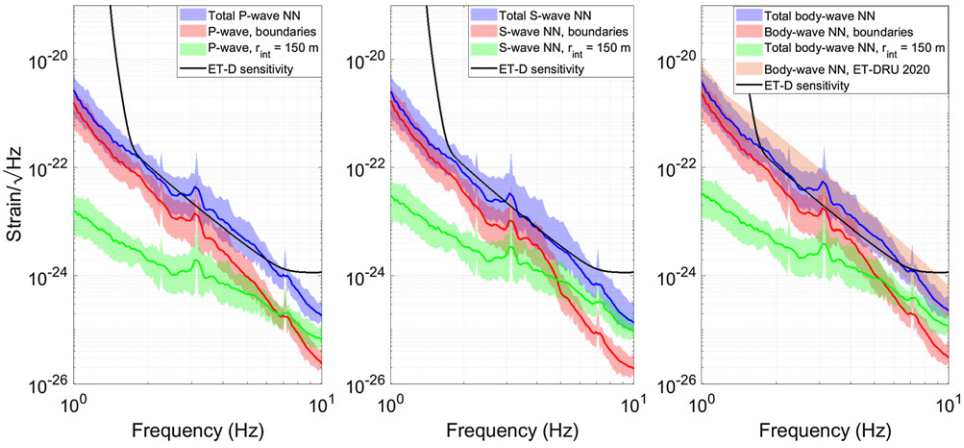

Figure 17. Estimate of the contribution of Newtonian noise from a random body-wave background to the sensitivity of Einstein Telescope at the EMR-site for test masses at 250 m depth enclosed in 10 m radius caverns. The black curve represents the ET-D design sensitivity. The left, middle and right panels show the P-wave, S-wave and total body-wave background contributions, respectively. The green curves represent the Newtonian noise due to displacements integrated over the volume up to a radius of 150 m around the mirror, while the blue curves represent the total noise due to body waves, integrated up to 10 km from the mirror. The red curves represent the contribution from mass movements across the boundaries between layers of different densities, most notably the boundary between air and soil. The shaded bands show the 10th and 90th percentiles. The orange band (right panel) shows the body-wave background Newtonian noise projected in the 2020-update of the Einstein Telescope design report [59].

displacements at an interface between media with different densities which is calculated separately. We can observe that this contribution is relatively large at low frequencies and is rapidly decreasing at higher frequencies, and that the relative importance of this term as a function of frequency is different for S- and P-waves. This can be understood by considering that for low frequencies and large wavelengths, the movements at the layer boundaries play a larger role. The surface contribution depends on vertical displacements with horizontal gradients. For P-waves this effect is maximal for a 45° angle with the vertical axis, whereas for S-waves the contribution is maximal for horizontally-traveling waves and zero for a purely vertically traveling wave. Maximal effects are expected for waves with wavelengths about twice the distance between the mirror and the layer boundary. For much smaller wavelengths the contributions from different patches of surface in the vicinity of the mirror cancel out. On the other hand for much longer wavelengths the gradient of the displacement in the direction of the interferometer arm is too small, surface displacements with small gradients tend to produce mainly vertical acceleration of the mirror. Indeed, we can notice in figure 17 that the S-wave surface contribution is relatively large around 4 Hz whereas the P-wave surface contribution is more important around 8 Hz.

In order to show the relative contributions to the Newtonian noise of the region nearby the test masses, we present in figure 17 also the results of the Newtonian-noise calculations up to a fixed radius of only 150 m. This integration radius is small enough that we do not cross a layer boundary; thus boundary terms do not contribute. We notice that for this region nearby the mirror, the S-wave contribution dominates. At 1 Hz, about 1% of the Newtonian noise arises from the volume with a radius of 150 m, whereas at 7 Hz this region already contributes half

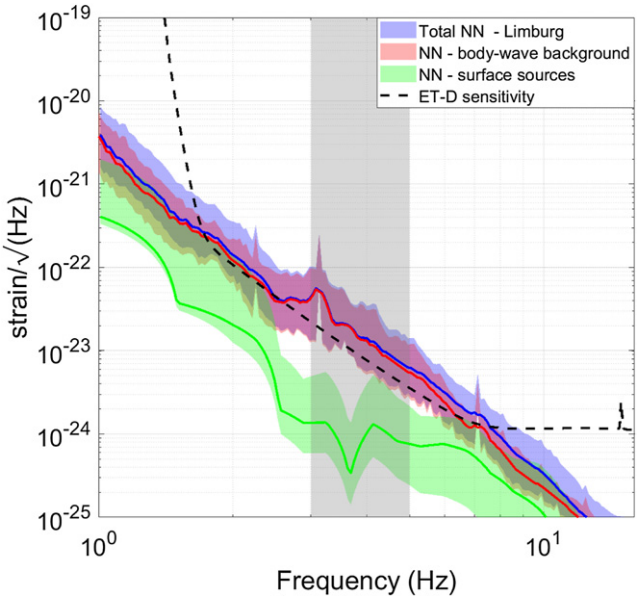

Figure 18. Newtonian-noise prediction for surface sources (green), body-wave background (red) and total (blue) to the sensitivity of Einstein Telescope at the EMR-site for test masses at 250 m depth enclosed in 10 m radius caverns. Solid curves show the mean, while the colored bands show the 10th and 90th percentiles. The ET-D sensitivity is represented by the dashed-black curve.

for S-waves. This contribution rises to 99% at 15 Hz. For P-waves, the inner 150 m contributes more than half of the Newtonian noise only for frequencies above 12 Hz. Nevertheless, these results show the importance of the inner region close to the mirror. The lower bound of the integration radius should start at the cavern walls around the mirror; if we would have chosen a larger cut-off radius of e.g. 1/4 wavelength (1125 m at 1 Hz) then a large fraction of the noise would not have been accounted for. For reliable results up to 20 Hz, one should not use a lower bound on the integration radius smaller than about 50 m.

4.6. Newtonian noise at the EMR-site in Limburg

The full Newtonian-noise estimate, i.e. the sum of the contribution from a random body-wave background and the contribution from surface excitations, is shown in figure 18. The solid-blue curve indicates the mean Newtonian-noise estimate, and the shaded band covers the region between the 10th and 90th percentiles. The spread in these estimates is caused by the spread in seismic activity. The contributions from surface sources and random body waves are indicated. The vertical gray band indicates the region where uncertainties may affect the surface contribution.

The mean Newtonian-noise estimate is up to a factor of 2 higher than the ET-D design sensitivity for frequencies up to about 8 Hz, and the body-wave background dominates. Although the anthropogenic noise is relatively strong in the Limburg region, the soft-soil surface layer traps and damps most of the surface activity and little noise penetrates to the depth of the mirrors. The relatively low wave speeds at the surface lead to many small patches of coherent movement and the total noise from the surface averages out to a large degree. Thus although the

PSD of the displacement field at the surface is significant, the geology helps to largely shield the underground mirrors from this noise source. While the surface contribution is effectively attenuated, the body-wave background exceeds the ET-D design sensitivity in the region of 3–6 Hz and a Newtonian-noise subtraction scheme may be required. For that, several underground sensors would be needed in the area around the mirrors, to characterize the body-wave spectrum and to be able to subtract part of the noise.

The calculated body-wave Newtonian noise is in reasonable accordance with the expectations in the updated ET design report [12] whereas the ambient noise from surface sources falls well below the expectation expressed in that report. Nevertheless, when one would aim for a Newtonian-noise contribution that falls below the sensitivity curve for at least 90% of the time, a cancellation scheme that reduces the body-wave background may be required. In this context we note that in our calculations, the body waves consist of plane waves with infinite coherence length. No dispersion, rescattering, or damping is included. We also used the highest wave speeds that were measured in [30], leading to maximal Newtonian noise in our model and hence to a conservative estimate.

5. Discussion and conclusion

Newtonian noise represents the dominant noise source for Einstein Telescope at low frequencies. To fulfill the ambitious sensitivity goals below about 10 Hz, it is important that Newtonian noise is well understood and modeled. In this work we estimate the seismically-induced Newtonian noise for the EMR Einstein Telescope candidate site in Limburg. The estimation is based on a full solution of the wave equation for a horizontally-layered geology, where the soil is excited in the vertical direction with surface sources that have a relative strength that matches the measured beampower. The geophysical model reproduces the measured fundamental-mode and first-overtone dispersion curves, $H{-}V$ spectral ratio, and surface and subsurface PSDs. Although the site is in close proximity to cities like Aachen, Liège, and Maastricht, the Newtonian-noise calculations demonstrate that the soft-soil on top of the hard-rock geology efficiently damps the produced anthropogenic noise, and that the EMR-site is in that respect compatible with Einstein Telescope's sensitivity requirements.

Deviations of the predictions of our model from the measurement results exist between 3 and 5 Hz, where the measured $H{-}V$ spectral ratio cannot be reproduced. This suggests that future modeling should include a more complete treatment of source mechanisms and allow lateral heterogeneity of the subsurface medium. In addition the inclusion of measured local material damping factors should be incorporated. Note that the differences between measured and simulated underground PSDs below 3 Hz suggest incompleteness of our horizontally-layered geophysical model.

At the depth of the borehole, contributions to the displacement field from a random body-wave background are non-negligible. We have measured this background and constructed a model by using an isotropic plane-wave spectrum that reproduces the measured background PSD. While the PSD of this random body-wave background increases to about 50% of the underground noise for frequencies above 4 Hz, it dominates the Newtonian-noise predictions for the EMR-site for frequencies over the entire frequency range and may require the realization of a Newtonian-noise subtraction scheme. It is recommended that future studies characterize the body-wave background by employing a network of subsurface and borehole tri-axial sensors, and model the Newtonian noise arising from it in detail, by including distant and underground sources that can reproduce the acquired seismic data at all depths.

A suitable site validation requires Newtonian-noise predictions that are based on seismic displacement fields that are derived from a geology model that includes realistic subsurface structures and seismic noise sources. Future Newtonian-noise models should go beyond the horizontally-stratified geology presented in this work to encompass complex, three-dimensional subsurface structures, realistic cavern shapes, damping factors derived from measurements, and a variety of source mechanisms that reproduce measurements of beamforming and H–V spectral ratios. While in the present work only a single location was studied, future work should be based on the modeling of all three corners of Einstein Telescope. Moreover, the Newtonian noise of Einstein Telescope's interferometers will be correlated, since test masses of multiple interferometers are located in each corner station of the observatory. The implications of these correlations remains to be investigated.

Acknowledgment

This work is part of the research program 'Advanced Virgo—Probing the dynamics of spacetime' with Project Number 680-45-113, which is (partly) financed by the Dutch Research Council (NWO). Moreover we thank NWO for the funding provided within the SENSEIS project: 'STW Open Technology Programme, Project 13338'.

Data availability statement

The data that support the findings of this study are available upon reasonable request from the authors.

ORCID iDs

Soumen Koley https://orcid.org/0000-0002-5793-6665
Jo van den Brand https://orcid.org/0000-0003-4434-5353
Xander Campman https://orcid.org/0000-0001-6482-1391

References

[1] Abbott B *et al* (LIGO Scientific and Virgo Collaboration) 2016 *Phys. Rev. Lett.* **116** 061102
[2] Abbott B *et al* (LIGO Scientific and Virgo Collaboration) 2016 *Phys. Rev. Lett.* **116** 241103
[3] Abbott B *et al* (LIGO Scientific and Virgo Collaboration) 2017 *Phys. Rev. Lett.* **118** 221101
[4] Abbott B *et al* (LIGO Scientific and Virgo Collaboration) 2017 *Astrophys. J. Lett.* **851** L35
[5] Abbott B *et al* (LIGO Scientific and Virgo Collaboration) 2017 *Phys. Rev. Lett.* **119** 141101
[6] Abbott B *et al* (LIGO Scientific and Virgo Collaboration) 2019 *Phys. Rev.* X **9** 031040
[7] Abbott R *et al* (LIGO Scientific and Virgo Collaboration) 2020 arXiv:2010.14527v1
[8] Abbott B *et al* (LIGO Scientific and Virgo Collaboration) 2017 *Phys. Rev. Lett.* **119** 161101
[9] Aasi J *et al* (LIGO Scientific Collaboration) 2015 *Class. Quantum Grav.* **32** 074001
[10] Acernese F *et al* (Virgo Collaboration) 2014 *Class. Quantum Grav.* **32** 024001
[11] Akutsu T A M *et al* (KAGRA Collaboration) 2019 *Nat. Astron.* **3** 30–40
[12] Abernathy M *et al* 2011 *Einstein Telescope Conceptual Design Study 'ET-0106C-10'* https://tds.virgo-gw.eu/?call_file=ET-0106C-10.pdf
[13] Maggiore M *et al* 2020 *J. Cosmol. Astropart. Phys.* JCAP04(2020)010
[14] 2020 Geo-services at the Central Bureau of Statistics, Netherlands https://cbsinuwbuurt.nl/

[15] van den Brand J 2019 *100 Years of General Relativity: Advanced Interferometeric Gravitational-Wave Detectors* vol 5 (Singapore: World Scientific) ch 6
[16] Accadia T *et al* 2011 *J. Low Freq. Noise Vib. Act. Control* **30** 63–79
[17] Weiss R 1972 *Gravitation research 105* (MIT: Research Laboratory of Electronics) http://dspace.mit.edu/bitstream/handle/1721.1/56271/RLE_gQPR_g105_gV.pdf?sequence=1
[18] Saulson P 1984 *Phys. Rev.* D **30** 732
[19] Fiorucci D, Harms J, Barsuglia M, Fiori I and Paoletti F 2018 *Phys. Rev.* D **97** 062003
[20] Harms J and Hild S 2014 *Class. Quantum Grav.* **31** 185011
[21] Beccaria M *et al* 1998 Relevance of Newtonian seismic noise for the VIRGO interferometer sensitivity *Class. Quantum Grav.* **15** 3339–362
[22] Beker M G *et al* 2011 *Gen. Relativ. Gravit.* **43** 623–56
[23] Hughes S and Thorne K 1998 *Phys. Rev.* D **58** 122002
[24] Harms J *et al* 2009 *Phys. Rev.* D **80** 122001
[25] Beker M, van den Brand J, Hennes E and Rabeling D 2011 *J. Phys.: Conf. Ser.* **363** 012004
[26] Beker M G 2013 Low-frequency sensitivity of next generation gravitational wave detectors *PhD Thesis* Vrije Universiteit Amsterdam
[27] Beker M *et al* 2016 *Lead. Edge* **35** 590–3
[28] Koley S *et al* 2018 Seismic noise characterization at a potential site for the Einstein telescope underground gravitational wave detector *80th EAGE Conf. Exhibition*
[29] Koley S, Bulten H J, Brand J. v. d., Bader M, Linde F and Beker M 2019 *First Break* **37** 83–90
[30] Koley S *et al* 2020 Surface and underground seismic characterization at Terziet in Limburg—the Euregio Meuse–Rhine candidate site for Einstein telescope (submitted)
[31] Koley S 2020 Sensor networks to measure environmental noise at gravitational wave detector sites *PhD Thesis* Vrije Universiteit Amsterdam
[32] Bader M 2021 Seismic and Newtonian noise modeling for advanced Virgo and Einstein telescope *PhD Thesis* Vrije Universiteit Amsterdam
[33] Innoseis 2013 *Innoseis* http://innoseis.com/ (accessed 20 July 2021)
[34] Deltares 2008 *Deltares—enabling delta life* https://deltares.nl/en/ (accessed 20 July 2021)
[35] Onderzoek T N 1932 *TNO—innovation for life—envision it | TNO* https://tno.nl/en/ (accessed 20 July 2021)
[36] Nederland E B 1973 *EBN: Energie Beheer Nederland—energising the transition* https://ebn.nl/en/ (accessed 20 July 2021)
[37] Chapman R E 1938 *Petroleum Geology* (*Developments in Petroleum Science*) vol 16 (Amsterdam: Elsevier)
[38] Schlumberger API https://glossary.oilfield.slb.com/en/Terms/a/api_gunit.aspx (accessed 20 July 2021)
[39] Advanced Logic Technology Bat A and Route de Niederpallen L8506 Redange sur Attert, Luxembourg QL40 ABI—Acoustic Borehole Imager—User Guide
[40] Doornenbal P 2017 *Uitwerkingen Boorgatmetingen Terziet Internal Report by Deltares*
[41] Schlumberger C, Schlumberger M and Leonardon E G 1932 *A.I.M.E Technical Publication* 462
[42] Klaja J and Dudek L 2016 *NAFTA-GAZ* **72** 3–14
[43] Peterson J 1993 Observations and modeling of seismic background noise *Open-file report* US Department of Interior Geological Survey 93–322
[44] KNMI 1993 Netherlands Seismic and Acoustic Network (Royal Netherlands Meteorological Institute (KNMI)) http://knmi.nl
[45] Koley S *et al* 2017 *First Break* **35** 71–8
[46] Woods J W and Lintz P R 1973 Plane waves at small arrays *Geophysics* **38** 1023–41
[47] Achenbach J 1984 *Wave Propagation in Elastic Solids* (*North-Holland Series in Applied Mathematics and Mechanics*) (Amsterdam: North-Holland)
[48] Foti S *et al* 2018 Guidelines for the good practice of surface wave analysis: a product of the InterPACIFIC project *Bull. Earthq. Eng.* **16** 2367–420
[49] Catello A, Hans-Balder H and Stratos Z 2004 Guidelines for the Implementation of the H/V Spectral Ratio Technique on Ambient Vibrations Measurements, Processing and Interpretation (European Commission)
[50] Shearer P M 2019 *Introduction to Seismology* (Cambridge: Cambridge University Press)
[51] Aki K and Richards P G 2002 *Quantitative Seismology* (Mill Valley, CA: University Science Books)
[52] Kausel E 2006 *Fundamental Solutions in Elastodynamics: A Compendium* (Cambridge: Cambridge University Press)

[53] Lo Presti D *et al* 1997 *Seismic Behaviour of Ground and Geotechnical Structures Conf. : Proc. 14th Int. Conf. Soil Mechanics and Foundations Engineering*
[54] Seats K *et al* 2010 On the composition of Earth's short-period seismic noise field *Bull. Seismol. Soc. Am.* **100** 606–17
[55] Punturo M 2012 *Advanced Virgo Sensitivity Curve Study Internal Virgo Note VIR-0073D-12*
[56] Acernese F *et al* 2014 Advanced Virgo: a second-generation interferometric gravitational wave detector *Class. Quantum Grav.* **32** 024001
[57] Hild S *et al* 2011 *Class. Quantum Grav.* **28** 094013
[58] Punturo M, Lück H and Beker M 2014 *Advanced Interferometers and the Search for Gravitational Waves* (Berlin: Springer)
[59] ET Steering Committee 2020 *ET Design Report Update 2020, Internal ET Documents ET-0007A-20*
[60] Press W H *et al* 2007 *Numerical Recipies—the Art of Scientific Computing* (Cambridge: Cambridge University Press)